

Self-pulsing and chaos in the asymmetrically-driven dissipative photonic Bose-Hubbard dimer: A bifurcation analysis

Jesús Yelo-Sarrión,¹ Francois Leo,¹ Simon-Pierre Gorza,¹ and Pedro Parra-Rivas^{1,2}

¹*OPERA-Photonique, Université libre de Bruxelles, 50 Avenue F. D. Roosevelt, CP 194/5 B-1050 Bruxelles, Belgium*

²*Dipartimento di Ingegneria dell'Informazione, Elettronica e Telecomunicazioni, Sapienza Università di Roma, via Eudossiana 18, 00184 Rome, Italy*

(Dated: February 9, 2022)

We perform a systematic study of the temporal dynamics emerging in the asymmetrically driven dissipative Bose-Hubbard dimer model. This model successfully describes the nonlinear dynamics of photonic diatomic molecules in linearly coupled Kerr resonators coherently excited by a single laser beam. Such temporal dynamics include self-pulsing oscillations, period doubled oscillatory states, chaotic dynamics, and spikes. The different states and dynamical regimes have been thoroughly characterized using bifurcation analysis. This analysis has allowed us to identify the main instabilities, i.e. bifurcations, responsible for the appearance of the previously stated dynamics.

I. INTRODUCTION

The emergence of self-sustained oscillations is commonly encountered in a variety of different fields ranging from chemistry and biology to physics and engineering [1, 2]. Some examples include the Belousov-Zhabotinsky reaction [3, 4], pulsation in Cepheid variable stars [2], or the oscillatory biochemical dynamics responsible for the cell division cycle [5]. In all these systems, the self-pulsing behavior emerges when varying a given parameter beyond a critical value, where time translation symmetry is broken. This oscillatory instability is known as a Hopf bifurcation [6, 7] and is key to understanding these dynamical phenomena. The self-sustained oscillations can evolve into much more complex dynamics. One example is chaos [8], which is present in different natural systems including weather and climate, fluid turbulent flow [9], and chemical reactions [10], to cite only a few.

Such rich temporal dynamics may also appear in optical systems. For example, self-pulsing has been found in second-harmonic generation [11], in lasers with continuous injected signals [12] or between coupled longitudinal modes [13] and, more recently, in coupled photonic cavities [14–17] or between counter-propagating beams in single Kerr cavities [18]. Furthermore, period-doubling and chaos have also been demonstrated (see e.g. Refs [19, 20]).

Lately, different works have focused on the dynamics of two coupled Kerr resonators: for the generation of optical frequency combs in integrated ring resonators in the anomalous [21] or the normal [22, 23] dispersion regime, as well as for parametric oscillation generation in coupled polariton [24] or fiber [25] cavities. This system is commonly known as *driven dissipative photonic Bose-Hubbard dimer* (PBHD) [26], in analogy with the open quantum boson system [27]. Advances on those different platforms have a broad range of applications ranging from spectroscopy [28] or metrology [29] to all-optical information storage [30]. Moreover, the addition of a second cavity has until now been proven useful to describe physical systems at the molecular level as shown

by Zhang et al. [31]. Those levels of control over tunable photonic systems pave the way to major advances in new unconventional information processing techniques such as all-optical [32] or quantum computing [33].

In a previous work, we found that self-pulsing oscillations appear in PBHDs when the driving is asymmetrical, i.e., when only one cavity is driven [25]. There, we focused on the self-pulsing dynamics, and we showed an excellent agreement between the experimental observations in coupled fiber cavities (in the normal dispersion regime) and the theoretical modeling. However, akin to Refs [15, 34], much richer dynamical regimes ranging from period doubled oscillatory states, temporal chaos, and the presence of spikes (i.e. homoclinic orbits) are expected. Thus, the main aim of this paper is to perform a systematic study of the dynamics, stability, and bifurcation structure of asymmetrically-driven dissipative PBHDs, applying well-known techniques of dynamical systems and bifurcation theory.

This article is organized as follows. In Section II we introduce the driven dissipative PBHD model, and we describe some of its characteristics, the 4D dynamical system associated with it, and the methodological approach that we will follow. Section III focuses on the steady states of the system, analyzing their linear stability and steady bifurcations for two coupling regimes. After that, in Section IV we perform a detailed bifurcation analysis of the previous coupling regimes, and we characterize the different dynamical scenarios. The origin of such dynamics is related to the presence of Hopf and homoclinic bifurcations. Later (see Section V), we study two homoclinic orbits of different types and present their main features. Section VI is devoted to elucidating the origin of the temporal chaos found in the system. Finally, we discuss our results and draw our conclusions in Section VII.

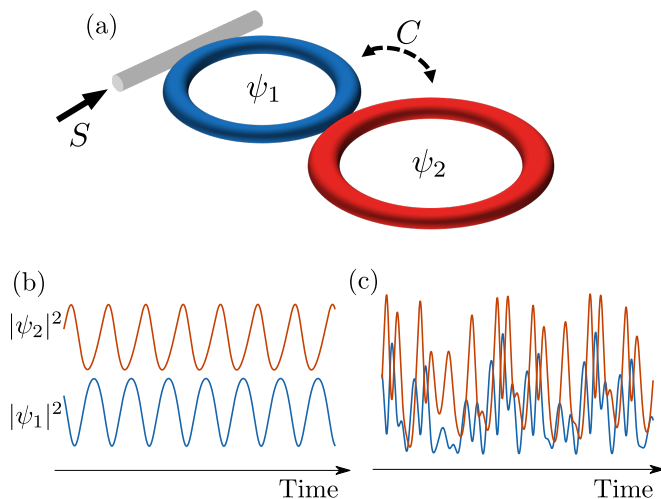


Figure 1. (a) Schematic view of an asymmetrically-driven dissipative PBHD. C represents the coupling between cavities and S the driving field. (b) Temporal traces of the cavity intensities $|\psi_{1,2}|^2$ in a self-pulsing regime. (c) Same as in (b) but in a chaotic dynamics regime.

II. THE ASYMMETRICALLY-DRIVEN DISSIPATIVE PHOTONIC BOSE-HUBBARD DIMER MODEL

Let us assume two identical cavities, mutually coupled via a middle coupler and coherently driven through a single input coupler [see Fig. 1(a)]. Regarding experiments, this scheme may be easier than with two pumps for which the relative phase between them must be precisely controlled. We here consider one-dimensional coupled cavities such as micropillar or photonic crystal cavities, but also coupled ring resonators (see discussion in Ref [25] regarding the dispersion). The dynamics of such PBHD can be described by two coupled one-dimensional normalized Lugiato-Lefever equations [35]

$$\begin{aligned} \frac{d\psi_1}{dt} &= [-1 + i(|\psi_1|^2 - \Delta)]\psi_1 + iC\psi_2 + S \\ \frac{d\psi_2}{dt} &= [-1 + i(|\psi_2|^2 - \Delta)]\psi_2 + iC\psi_1 \end{aligned} \quad (1)$$

where the time $t = t'\kappa/T_R$ with t' the laboratory time, T_R the round-trip time and κ the cavity loss coefficient (excluding the middle coupler). The detuning from the closest (single cavity) resonances is $\Delta = \delta/\kappa = (m2\pi - \varphi)/\kappa$, where φ is the round-trip linear phase shift and m an integer number. $C = \sqrt{\theta_{12}}/\kappa$, where θ_{12} is the transmission coefficient of the coupler between the cavities. Finally $\psi_j = A_j\sqrt{\gamma L/\kappa}$, ($j = 1, 2$), $S = i\sqrt{P_p\gamma L\theta_p/\kappa^3}$, where A_j are the field amplitudes normalized such that the intracavity powers (expressed in watts) are given by $|A_j|^2 = P_j$. P_p is the driving power, θ_p is the transmission coefficient of the input coupler, γ is the nonlinear parameter of the waveguide and L is the length of the resonators. The normalization scheme follows the one

proposed in Ref. [30].

In order to study this system we are going to apply two different procedures: the direct numerical integration of Eqs. (1), using a split-step algorithm, and the numerical path-continuation [36, 37] of the different states of the system using the free software continuation package AUTO-07p [38]. This last approach allows us to characterize the bifurcation structure and stability of the different static and periodic dynamical states as a function of the parameters of the system. For the periodic states, Floquet analysis is applied [39].

To perform numerical parameter continuation, it is convenient to recast the complex dynamical system (1) into the 4D system

$$\begin{aligned} \frac{du_1}{dt} &= -u_1 - (u_1^2 + v_1^2 - \Delta)v_1 - Cv_2 + S \\ \frac{dv_1}{dt} &= -v_1 + (u_1^2 + v_1^2 - \Delta)u_1 + Cu_2 \\ \frac{du_2}{dt} &= -u_2 - (u_2^2 + v_2^2 - \Delta)v_2 - Cv_1 \\ \frac{dv_2}{dt} &= -v_2 + (u_2^2 + v_2^2 - \Delta)u_2 + Cu_1, \end{aligned} \quad (2)$$

where $\psi_j = u_j + iv_j$, for $j = 1, 2$. As control parameters we consider the pump intensity S , the coupling constant C , and the phase detuning Δ .

This system supports self-pulsing dynamics, i.e., periodic oscillations in time, as schematically shown in Fig. 1(b). Through the modification of suitable parameters, these oscillations can suffer different transitions leading to more complex dynamics. One example of such complexity, corresponding to chaos, is depicted in Fig. 1(c). In what follows we will unveil the features of these states and the transition that they may encounter.

III. STEADY-STATES, LINEAR STABILITY, AND THEIR PHASE DIAGRAM

The steady-states of the system correspond to the fixed points or equilibria $\psi_e = (\psi_1^e, \psi_2^e) = (u_1^e, v_1^e, u_2^e, v_2^e)$ of equations (1), such that $d\psi/dt = 0$. They are solution of the algebraic system

$$\begin{aligned} [-1 + i(|\psi_1|^2 - \Delta)]\psi_1 + iC\psi_2 + S &= 0 \\ [-1 + i(|\psi_2|^2 - \Delta)]\psi_2 + iC\psi_1 &= 0 \end{aligned} \quad (3)$$

which leads to

$$\begin{aligned} I_1 + (I_1 - \Delta)^2 I_1 - C^2 I_2 - S^2 + 2CSv_2 &= 0 \\ I_2 + (I_2 - \Delta)^2 I_2 - C^2 I_1 &= 0 \end{aligned} \quad (4)$$

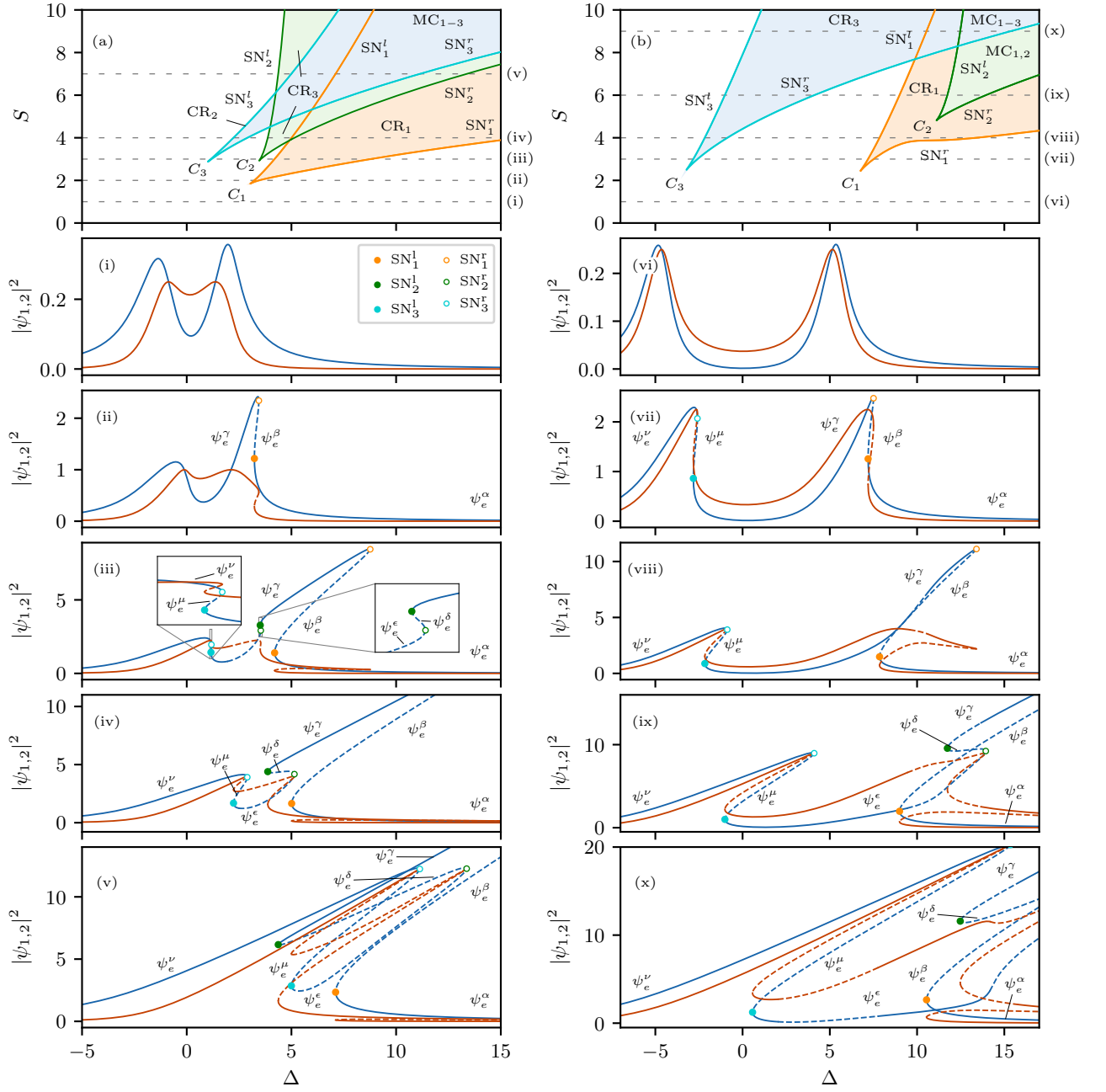


Figure 2. Steady-state phase diagrams in the weakly and strongly couple regimes. (a) shows the (Δ, S) -phase diagram for $C = 1.5$. The bifurcation diagrams shown in panels (i)-(iv) correspond to slices of constant S [see dashed horizontal lines in (a)]. They represent the intensities $|\psi_1|^2$ (blue) and $|\psi_2|^2$ (red) as a function of Δ . From top to bottom the values are $S = 1, 2, 3, 4$ and 7 . (b) shows the (Δ, S) -phase diagram for $C = 5$. Panels (v)-(viii) are slices of panel (b) for the constant values $S = 1, 3, 4, 6$ and 9 (from top to bottom). Solid and dashed lines represent stable and unstable equilibria (ψ_e^i) respectively. In (a) and (b) different coexistence regions (CR_j), and multi-coexistence regions (MC_j) are depicted as well as the static bifurcations of the equilibria: saddle-node $SN_i^{l,r}$ and cusp C_i .

The linear stability of these points is obtained from the local dynamics of (2) around ψ_e , which is solely determined by the eigenvalues λ of the Jacobian \mathcal{J} of the system at that point. The complicated form of Eq. (4) prevents the possibility of extracting an analytical expression of the eigenvalues of the system. However, the equi-

libria and their stability can be easily computed numerically through the path-continuation algorithm [36, 37].

When two identical cavities are coupled, each resonance is split in two peaks. These peaks correspond to the excitation of the hybridized modes, often called the antibonding-like ($\Delta < 0$) and the bonding-like ($\Delta > 0$)

modes of the photonic dimer. The detuning separation between them is equal to $2C$ and can thus be freely adjusted through the cavity coupling strength. In this study we consider two main dynamical regimes corresponding to the *weakly-coupled* scenario ($C = 1.5$) for which the splitting is only slightly larger than the resonance width, and the *strongly-coupled* scenario ($C = 5$), showing a much larger peak separation. Hereafter we refer to them as WC and SC regimes respectively. The coupling constant that we consider in the WC regime is similar to the experimental value considered in our previous work [25]. In the SC, while the encountered dynamics are similar, the bifurcation diagram is much more complex. In what follows, we study these two regimes separately. Their steady-state bifurcation structure is summarized in the diagrams plotted in Fig. 2.

A. Steady states in the weakly coupled regime

Figure 2(a) shows the steady-state phase diagram in the (Δ, S) -parameter space for $C = 1.5$. Slices of such diagram, for increasing values of S , are depicted in Figs. 2(i)-(iv) where the intensities $|\psi_{1,2}|^2$ are plotted against Δ . The linear stability of these states is marked using solid (dashed) lines for stable (unstable) equilibria, and only steady-state bifurcations are labeled.

The two resonances are quite overlapped in the WC regime as can be seen for $S = 1$ [see Fig. 2(i)] for which the system is still close to the linear regime. At this driving level, the resonances are only slightly asymmetric, a single equilibrium exists for each given value of Δ and it is linearly stable.

Increasing S [see Fig. 2(ii) for $S = 2$], the asymmetry between the resonances increases, yielding a larger right resonance in detriment of the left one. The right resonance undergoes a cusp or hysteresis bifurcation C_1 , where a pair of folds, or turning points, are created, leading to the tilted shape. [39] These folds correspond to saddle-node bifurcations that we label $\text{SN}_1^{l,r}$. At these bifurcations, a stable node equilibrium and an unstable saddle collide and disappear. This transition leads to the coexistence of three different equilibria $\psi_e^{\alpha,\beta,\gamma}$, where ψ_e^α and ψ_e^γ are nodes (i.e., stable), whereas ψ_e^β is a saddle [39]. The separation in Δ between SN_1^l and SN_1^r defines the *coexistence region* CR_1 (see light orange area).

Further increasing S , both resonances tilt to the right due to the effect of the nonlinearity and two new cusp bifurcations occur [see Figs. 2(a) and 2(iii) for $S = 3$]: C_2 on the right resonance, and C_3 on the left one. In C_2 , $\text{SN}_2^{l,r}$ are created. These pair of bifurcations leads to the equilibria ψ_e^δ and ψ_e^ϵ (see close-up view) which are both unstable and coexist in CR_2 . C_3 creates $\text{SN}_3^{l,r}$, and the two new equilibria ψ_e^μ and ψ_e^ν associated with the left resonance appear. Between $\text{SN}_3^{l,r}$ the bistability region CR_3 is created.

In Fig. 2(iv) we plot the bifurcation diagram for $S = 4$.

For this value, the tilting of the resonance is much more prominent, and the bistability interval between ψ_e^α and ψ_e^γ has increased considerably. For increasing values of S , the separation between the pairs $\text{SN}_1^{l,r}$, $\text{SN}_2^{l,r}$, $\text{SN}_3^{l,r}$ increases [see Fig. 2(a)], and a *multi-coexistence region* appears between SN_1^l and SN_3^r that we label MC_{1-3} . An example of this situation is depicted in Fig. 2(v) for $S = 7$. Here we can see how both resonances are overlapped and lead to tristability and an effective single resonance.

B. Steady states in the strongly coupled regime

Let us now focus on a scenario with a higher coupling and fix $C = 5$. Figure 2(b) shows the phase diagram for that coupling, and Figs. 2(v)-(x) the bifurcation diagrams for some relevant values of S . In the linear regime the two resonances are now well separated. At $S = 1$, they are still almost symmetric [see Fig. 2(iv)].

Increasing S , the system encounters C_1 and C_3 almost simultaneously, where the pairs $\text{SN}_1^{l,r}$ and $\text{SN}_3^{l,r}$, together with the equilibria $\psi_e^{\alpha,\dots,\epsilon}$ are created as seen in Figs. 2(b). These bifurcations define the coexistence regions CR_1 and CR_2 . An example of this configuration is plotted in Fig. 2(vii) for $S = 3$, where different equilibria are depicted. For this value of S , the resonance already tilts slightly to the right.

The configuration suffers an interesting modification for $S = 4$ as shown in Fig. 2(viii). For this value, the right resonance has just merged with an isola in a necking bifurcation (not shown here) [40]. In this bifurcation, SN_1^r and the left fold of the isola SN_1^l collide and the equilibria branches reconnect, enlarging in this way the arm of the right resonance which now extends until SN_1^r [relabelled as SN_1^l in Figs. 2(a) and 2(viii) for clarity]. This type of merging is illustrated in detail in [25].

Moving up in Fig. 2(b), C_2 occurs and $\text{SN}_2^{l,r}$ are created. After this point, the configuration is like the one depicted in Fig. 2(ix) for $S = 6$. For this value of S , SN_1^l and SN_1^r are far apart, and the right resonance extends to larger values of Δ .

For $S = 9$ [see Fig. 2(x)], the left resonance has grown significantly as SN_3^l overpasses SN_1^l and SN_2^l . At this stage, a tristable regime appears. Tristability persists for even larger values of S , where an effective single resonance can emerge similarly to the case shown in Fig. 2(v). Here we can identify two main regions of multi coexistence that are labeled $\text{MC}_{1,2}$ and MC_{1-3} .

IV. DYNAMICAL REGIMES AND BIFURCATION STRUCTURE

In the previous section, we have focused on the steady-state equilibria and their steady bifurcations. As previously stated, self-pulsing oscillations and chaos may emerge in the system [see Figs. 1(b) and (c)]. In this section, we expand the previous analysis by studying the

dynamical behavior of the system and present a systematic study of the bifurcation structure associated with such states in the WC and SC regimes.

A. Dynamics in the weakly coupled regime

The phase diagram shown at the top of Fig 3 summarizes the main dynamical regimes and bifurcation lines of the system for $C = 1.5$. To understand such a diagram we slice it as shown by the horizontal and vertical dashed lines. Each of these lines corresponds to one of the bifurcation diagrams shown below. The slices with constant S are plotted in Figs. 3(i)-(iii), whereas those with constant Δ are depicted in Fig 3(iv)-(vi).

Figure 3(i) shows a close-up view of Fig. 2(ii) around the bistability region between ψ_e^α and ψ_e^γ for $S = 2$. Upon increase of S , the Hopf bifurcation (H) line plotted in Fig. 3(a) is crossed, and the system enters a self-pulsing regime (see red shadowed region) characterized by single period oscillations like those shown in Fig. 1(b). An example of this configuration is plotted in Fig. 3(ii) for $S = 2.5$, where H is crossed at two points H^a and H^b . The periodic oscillations emerge supercritically from H^a and with small amplitude from the left. The maximum and minimum of the oscillation are represented using red solid lines. Increasing Δ , the oscillation amplitude grows until suddenly it dies out at H^b on the right. This dramatic change of the oscillation amplitude in phase space is called *canard explosion* [41], and is related to type II excitability [42, 43].

For $S = 3.5$, the situation is shown in Fig. 3(iii). For this value, the equilibria ψ_e^δ , ψ_e^ϵ , and ψ_e^μ , ψ_e^ν , coexist. Furthermore, periodic oscillations persist. On the left, they still emerge from H^a . On the right, however, they die on a *homoclinic* (Hom) bifurcation [7, 44], while only steady states persist for larger values of Δ .

The homoclinic bifurcations are global bifurcations related to the collision of a cycle (i.e. a periodic orbit Γ) with an equilibrium, and are characterized by the divergence of the cycle's period [44]. At the bifurcation point, the limit cycle Γ becomes a homoclinic orbit γ , i.e., a trajectory in the phase space which is bi-asymptotic to the equilibrium. This bifurcation is associated with type-I excitability [42].

In the phase diagram of Fig. 3(a), the Hom bifurcation corresponds to the black solid line. To track numerically this line in the (Δ, S) -parameter space we have used the homoclinic continuation HOMCONT extension of AUTO-07p [45]. We will focus our attention on this type of bifurcations in Sec. V.

We can also analyze the (Δ, S) -phase diagram considering slices of constant Δ . The resulting bifurcation diagrams are shown in Figs. 3(iv)-(vi), where $|\psi_1|^2$ is plotted as a function of S . In Fig. 3(iv) [$\Delta = 2$] bistability exist between SN_3^l and SN_3^r , and the limit cycle Γ emerges and dies at H^a and H^b respectively. For this slice, bistability exists between ψ_e^ϵ and ψ_e^ν .

Increasing Δ [see Fig. 3(v) for $\Delta = 3$], the bistability interval is now bound by H^b and SN_3^r . Γ increases drastically its amplitude and undergoes several secondary bifurcations such as saddle-node bifurcation of periodic orbits (SNP), also known as fold of cycles, and period-doubling bifurcations (PD) [39, 46]. For clarity, we do not plot these bifurcation lines in the phase diagram of Fig. 2(a). The presence of a PD may suggest the existence of chaotic dynamics emerging from a period-doubling cascade [8]. We will analyze the chaotic dynamics of this system in Sec. VI.

In Fig. 3(vi) [$\Delta = 4$] we plot the bifurcation diagram after the occurrence of C_2 and C_1 . Here, the bistability between H^b and SN_3^r reduces drastically (see close-up view), and the pair of bifurcations $\text{SN}_2^{l,r}$ and $\text{SN}_1^{l,r}$ appear. Between the last two bifurcations, a new bistability range emerges, where ψ_e^α and ψ_e^γ coexist. This slice cuts Hom in three different points that we label $\text{Hom}^{a,b,c}$, respectively. Periodic oscillations exist between Hom^a and Hom^b , and between Hom^c and H^b .

The region in-between the H and Hom lines in the (Δ, S) -parameter space [see the red shadowed area in Fig. 3(a)] is the dynamical region of the system where self-pulsing and other dynamical states (e.g., chaos) may emerge.

The H and Hom bifurcations arise from a pair of codimension-two Takens-Bodganov (TB) bifurcations [6, 39] which occur at SN_2^l and SN_3^l . For the range of parameters considered here, we only observe TB_1 [see a close-up view in Fig. 3(a)]. At this bifurcation, the linearized dynamics of the system has two zero eigenvalues $\lambda_{1,2} = 0$ (with algebraic multiplicity 2), for this reason, it is also known as a double zero bifurcation [6]. The periodic oscillations arise from this point with an infinite period, which becomes finite as H separates from Hom.

B. Dynamics in the strongly coupled regime

Let us now analyze the bifurcation structure of the system in the SC regime. The (Δ, S) -phase diagram plotted in Fig. 4(a) summarizes the main dynamical regions of the system for $C = 5$. One of the main differences is the presence of two distinct, but connected, single-period oscillatory regimes (see red shadowed regions bounded by H_1 and H_2), which were fused for smaller values of C [see phase diagram in Fig. 3(a)]. The steady-state bifurcations (i.e., the saddle-nodes) are the same as those already plotted in Fig. 2(b). Besides the two Hopf bifurcations H_1 and H_2 , two $\text{SNP}_{1,7}$, several period-doubling bifurcations PD_{1-3} , and two homoclinic bifurcations $\text{Hom}_{1,2}$ are drawn.

To understand this diagram we take several slices at constant S . The corresponding bifurcation diagrams are shown in Fig. 4(i)-(v). Let us first analyze the bifurcation structure and dynamics around the right nonlinear resonance emerging from C_1 . The modification of the dynamical scenario around this resonance is depicted in

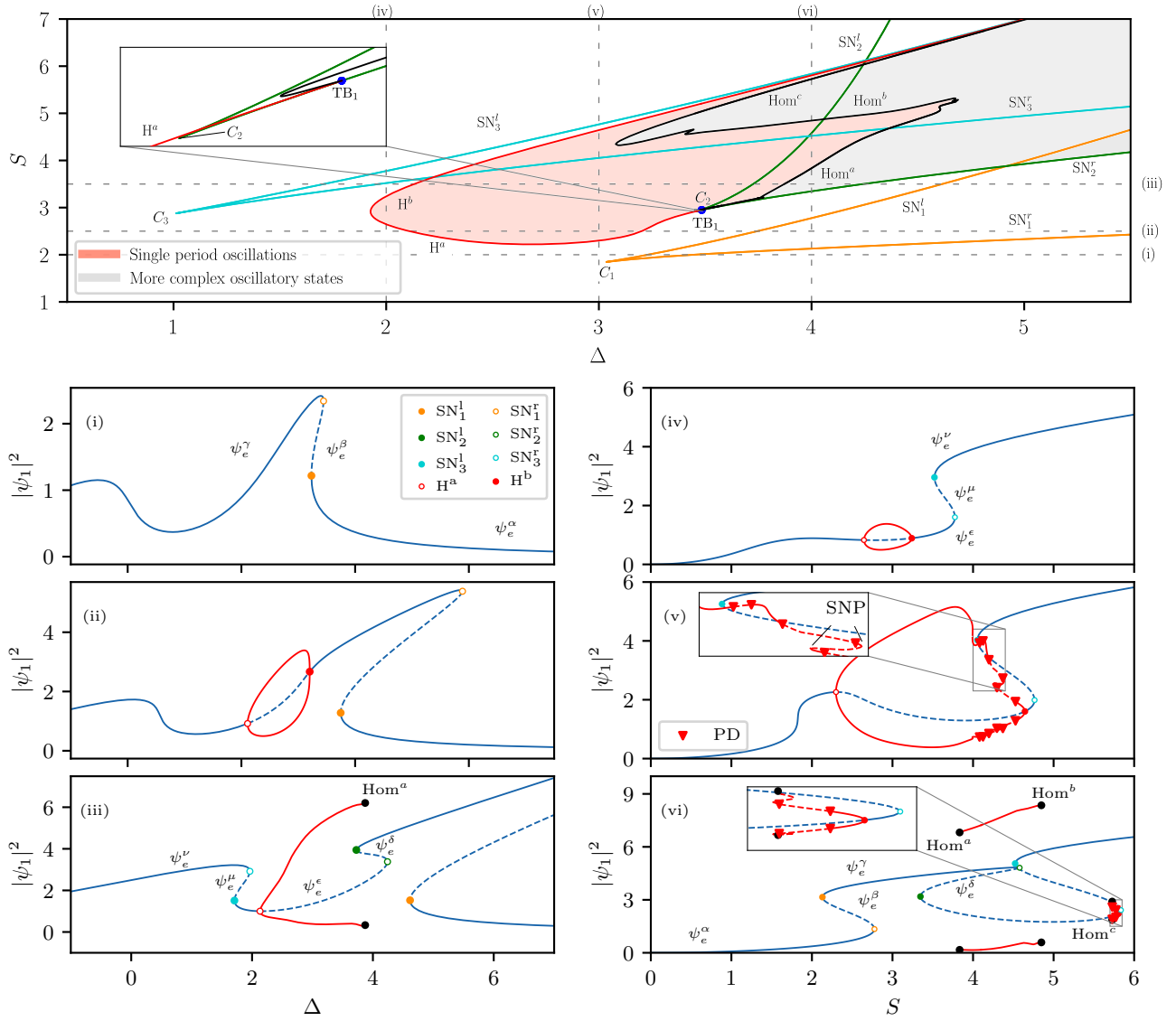


Figure 3. (a) Phase diagram in the (Δ, S) -parameter space for $C = 1.5$ showing the main dynamical regions and bifurcations of the system: saddle-node of the steady state $SN_i^{l,r}$, cusp C_i , Hopf $H^{a,b}$, saddle-node of periodic oscillatory states SNP, homoclinic $Hom^{a,b}$, and Takens-Bogdanov TB_j . The red shadowed region corresponds to self-pulsing dynamics. The vertical and horizontal dashed lines correspond to the bifurcation diagrams shown in panels (i)-(iii) for constant S ($= 2, 2.5$ and 3.5), and panels (iv)-(vi) for constant Δ ($= 2, 3$ and 4). Stable and unstable equilibria (ψ_e^i) are plotted with solid and dashed lines respectively. The red lines represent the maxima and minima of the periodic oscillations.

Figs. 4(i)-(iv).

The diagram shown in Fig. 4(i) [$S = 4.5$] intersects H_2 at two points, labeled $H_2^{a,b}$, from where periodic oscillations arise. Due to the complexity of this scenario, we have used different colors for each of the limit cycles. In red we plot the maximum and minimum of the oscillation arising from H_2^a and in orange the one emerging from H_2^b . The linear stability of these limit cycles is depicted with solid lines for stable states, and dashed lines for the unstable ones. The limit cycle arising from H_2^a , hereafter Γ_a , undergoes a pair of secondary $SN_{1,2}$. For simplicity, we only plot SN_1 in Fig. 4(a). Increasing Δ , Γ_a encounters

the homoclinic bifurcation Hom_1^a where it is destroyed. The limit cycle originating from H_2^b , however, quickly undergoes a PD_1 bifurcation when decreasing Δ . We label this oscillatory state Γ_b . Eventually, the extrema of Γ_b develop a spiral structure which collapses to the Hom_1^b (see close-up view). This spiral behavior is typical of one type of homoclinic bifurcation [34]. Between Hom_1^a and Hom_1^b the only attractor of the system is ψ_e^α .

With increasing S [see Fig. 4(a)], the period-doubling bifurcation line PD_2 appears, and $SN_2^{l,r}$ are created at C_2 . The bifurcation diagram in this regime is like the one shown in Fig. 4(ii) for $S = 5$. For this value, PD_2

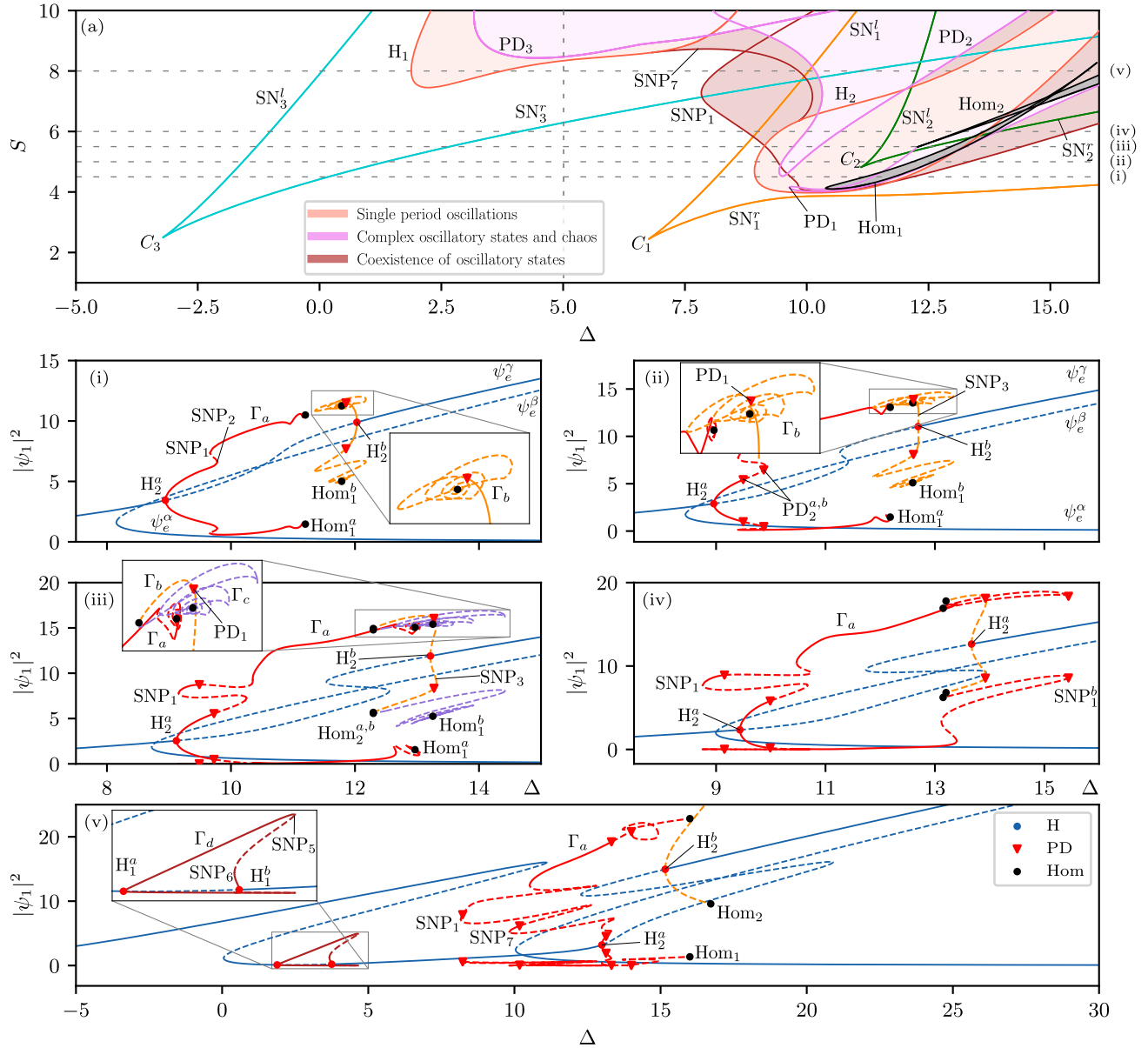


Figure 4. Bifurcation structure for $C = 5$. (a) shows the phase diagram in the (Δ, S) -parameter space which illustrates the different dynamical regions and main bifurcations of the system: saddle-node of the steady-state $SN_i^{l,r}$, Hopf $H_{1,2}^{a,b}$, period-doubling $PD_i^{a,b}$, saddle-node of periodic oscillatory SNP_i , and homoclinic $Hom_{1,2}^{a,b}$. The horizontal dashed lines correspond to the bifurcation diagrams shown below, where $|\psi_1|^2$ is plotted as a function of Δ for $S = 4.5$ (i), 5 (ii), 5.5 (iii), 6 (iv) and 8 (v). The vertical dashed line corresponds to the bifurcation diagram shown in Fig. 8(a). In diagrams (i)-(v) solid (dashed) lines represent stable (unstable) equilibria (ψ_e^i) and limit cycles (Γ_i).

is sliced in two points, namely $PD_2^{a,b}$. With increasing Δ , Γ_a increases its amplitude, and eventually starts to spiral around Hom_1^a , where it is finally destroyed (see close-up view). Γ_b now emerges from H_2^b subcritically and stabilizes at SNP_3 before losing stability in PD_1 . Once this point is crossed, Γ_b describes a large spiral, before dying at Hom_1^b .

Figure 4(iii) shows the modification of the bifurcation diagram for $S = 5.5$. As $SNP_{1,2}$ are further apart, we can

see that stable oscillations of different amplitudes coexist in a narrow Δ interval in-between SNP_1 and the closest PD_2 point. However, the main difference is seen in the right part of the diagram. Γ_b emerges subcritically from H_2^b (see orange curve), and becomes stable at SNP_3 , just before being destabilized at PD_1 once more. However, in contrast to Fig. 4(ii), Γ_b does not describe a spiral around Hom_2^b but approaches that point monotonically. Very close to Hom_2^a , the cycle is created again at Hom_2^b ,

leading to the purple unstable curve Γ_c . This cycle is mainly unstable and spirals around Hom_1^b , where it is finally destroyed. A detailed study of this configuration is presented in Sec. V (see Fig. 5).

The bifurcation structure is very similar for $S = 6$ [see Fig. 4(iv)], with larger separations between the different saddle-node bifurcations. For simplicity, we have omitted the solution branches associated with Γ_c . For this value of S , $\text{Hom}_1^{a,b}$ occurs near one another. From a stability perspective, everything is equivalent to the case for $S = 5.5$.

We have discussed so far the bifurcation structure of the dynamical states emerging from H_2 (i.e. around the right resonance) as this bifurcation is first encountered when S is increased. However, for S larger than ≈ 7.5 , complex nonlinear dynamics also occur around the left nonlinear resonance. Figure. 4(v) illustrates a slice of Fig. 4(a) for $S = 8$, where both resonances are plotted. For this value, the bifurcation structure of the oscillations around the tilted right resonance becomes much more complex. Regarding the tilted left one, a new oscillatory state Γ_d emerges supercritically from H_1^a . Γ_d increases its amplitude with Δ and becomes unstable at SNP_5 . From H_1^b the periodic orbit also emerges supercritically, although it undergoes SNP_6 where it becomes unstable. These oscillations correspond to the instability mechanism reported in Refs. [24, 47] in which the nonlinearity shifts the resonances so as to allow for a resonant four-wave-mixing process with signal and idler photons respectively on the bonding- and antibonding-like mode of the dimer. On the contrary, the parametric instability originating from H_2 involves signal and idler photons on both the bonding- and antibonding-like modes (See Supplemental Material of Ref [25]).

From each PD bifurcation, a period-doubling cascade can be triggered, potentially leading to chaotic dynamics [8]. Period doubled states and chaotic ones will be analyzed in detail in Sec. VI.

For $C = 5$, neither the Hopf nor the homoclinic bifurcations emerge from TB points, differently to the case in Sec. III for $C = 1.5$. Regarding, $H_{1,2}$ we have found that they extend to large values of Δ and S (far from the range of applicability of the model), and no signs have been found about their relation with TB points. Similarly, we have established that Hom_1 forms a close loop in the parameter space, and thus they are detached from any codimension-two point.

V. HOMOCLINIC BIFURCATIONS

In previous sections, we have found that for some ranges of parameters the periodic oscillations emerging at Hopf bifurcations die out in global homoclinic bifurcations. These bifurcations take place when a limit cycle Γ collides with an unstable (hyperbolic) equilibrium for some set of parameters. As the cycle approaches the unstable equilibrium, its period drastically grows, diverg-

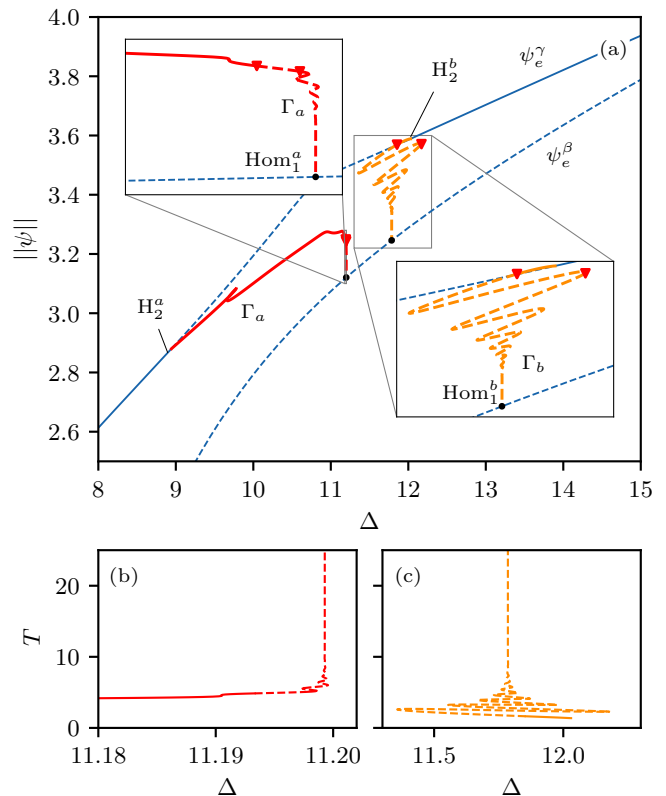


Figure 5. Shilnikov homoclinic bifurcations for $C = 5$ and $S = 4.5$. (a) Close-up view of the diagram shown in Fig. 4(i) around $\text{Hom}_1^{a,b}$. Here we plot $\|\psi\|$ as a function of Δ . (b) shows the divergence of the period T of Γ_a at Hom_1^a , and (c) the damped oscillatory modification of the period of Γ_b with Δ around Hom_1^b . See Fig. 4 for the definition of the labels.

ing at Hom [7, 39]. At this point, the periodic solution Γ becomes a homoclinic orbit γ , i.e., a closed trajectory linking the unstable equilibrium with itself. Depending on the nature of such equilibrium, different types of Hom bifurcations take place [7, 48]. In our system we have identified two types corresponding to the following conditions:

- When the leading eigenvalues $\lambda_{1,2}$ of the Jacobian \mathcal{J} are real (i.e. $\lambda_{s,u} = a_{s,u} \in \mathbb{R}$) such that $a_s < 0 < a_u$, the Hom orbit γ is biasymptotic to a saddle equilibrium, and the Hom bifurcation is commonly called *saddle-loop* Hom bifurcation [42].
- If the leading eigenvalues of \mathcal{J} are one real and one complex conjugate pair (i.e., $\lambda_s = a_s \pm i\omega_s$ and $\lambda_u = a_u$), with $a_s < 0 < a_u$, and $\omega_s > 0$, the Hom orbit is biasymptotic to a saddle-focus equilibrium, and the bifurcation is known as saddle-focus Hom bifurcation or *Shilnikov* bifurcation [44]. A relevant parameter describing the nature of these points is the *saddle-index* quantity [7]

$$\delta \equiv -\text{Re}[\lambda_s]/\lambda_u. \quad (5)$$

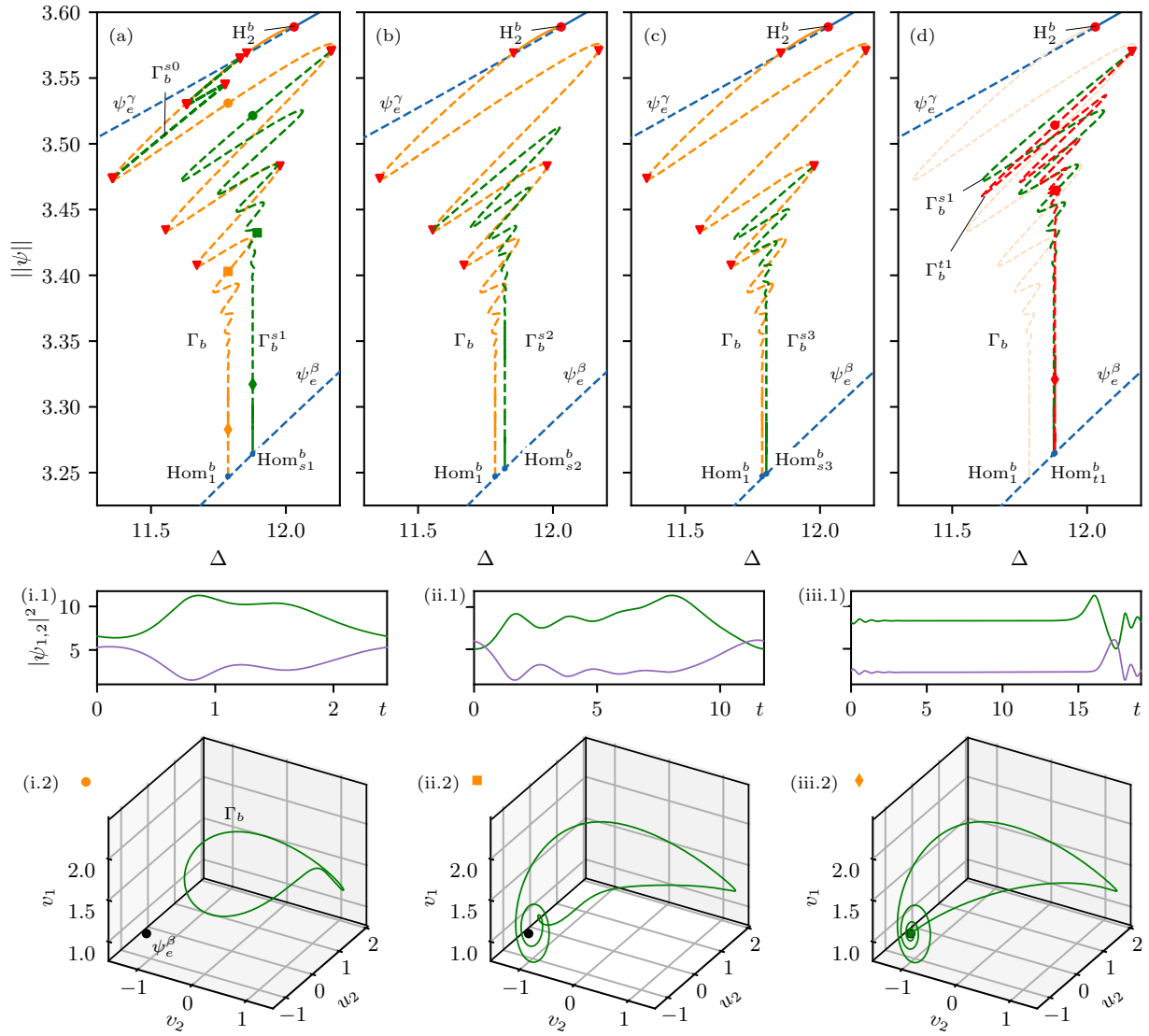


Figure 6. Bifurcation diagram of the principal and subsidiary periodic orbits close to Hom_1^b for $C = 5$ and $S = 4.5$. (a) shows the bifurcation curve associated with the principal orbit Γ_b emerging from H_2^b and dying at Hom_1^b . Two subsidiary branches Γ_b^{s0} and Γ_b^{s1} , are also plotted. Γ_b^{s1} connects with ψ_e^β at Hom_{s1}^b . (b) shows the principal orbit Γ_b and the subsidiary curve arising from the fourth PD bifurcation. We label with orbits and its bifurcation curve Γ_b^{s2} . In (c) we plot Γ_b and another subsidiary orbit Γ_b^{s3} which dies at Hom_{s3}^b . (d) shows the subsidiary curve and Γ_b^{s1} , and the tertiary oscillatory state Γ_b^{t1} arising from it. The modification of the oscillatory state Γ_b descending its bifurcation curve [see \bullet , \blacksquare , \blacklozenge in (a)] is depicted in panels (i)-(iii) where the temporal trace and 3D attractors are depicted.

When $\delta > 1$, the saddle-focus homoclinic orbit is said to be *tame* [44] and the dynamics are essentially the same as in the saddle-loop case. In contrast, when $\delta < 1$ the homoclinic orbit is called *wild* and the dynamics of the system around it is richer. In particular, there is an infinite number of SNP and period-doubling bifurcations in any parameter interval containing the bifurcation [7, 44, 46].

A. Saddle-focus (Shilnikov) homoclinic bifurcation

Most of the homoclinic bifurcations and orbits appearing in our system are of the Shilnikov type. The bifurcation diagram plotted in Fig. 5(a) shows the appearance of these bifurcations for $C = 5$ and $S = 4.5$. It consists of a close-up view of the diagram shown in Figs. 4(i). For more clarity, we plot the L_2 -norm

$$\|\psi\| \equiv \sqrt{T^{-1} \int_0^T (|\psi_1(t)|^2 + |\psi_2(t)|^2) dt}, \quad (6)$$

Let us analyze these bifurcations in our case.

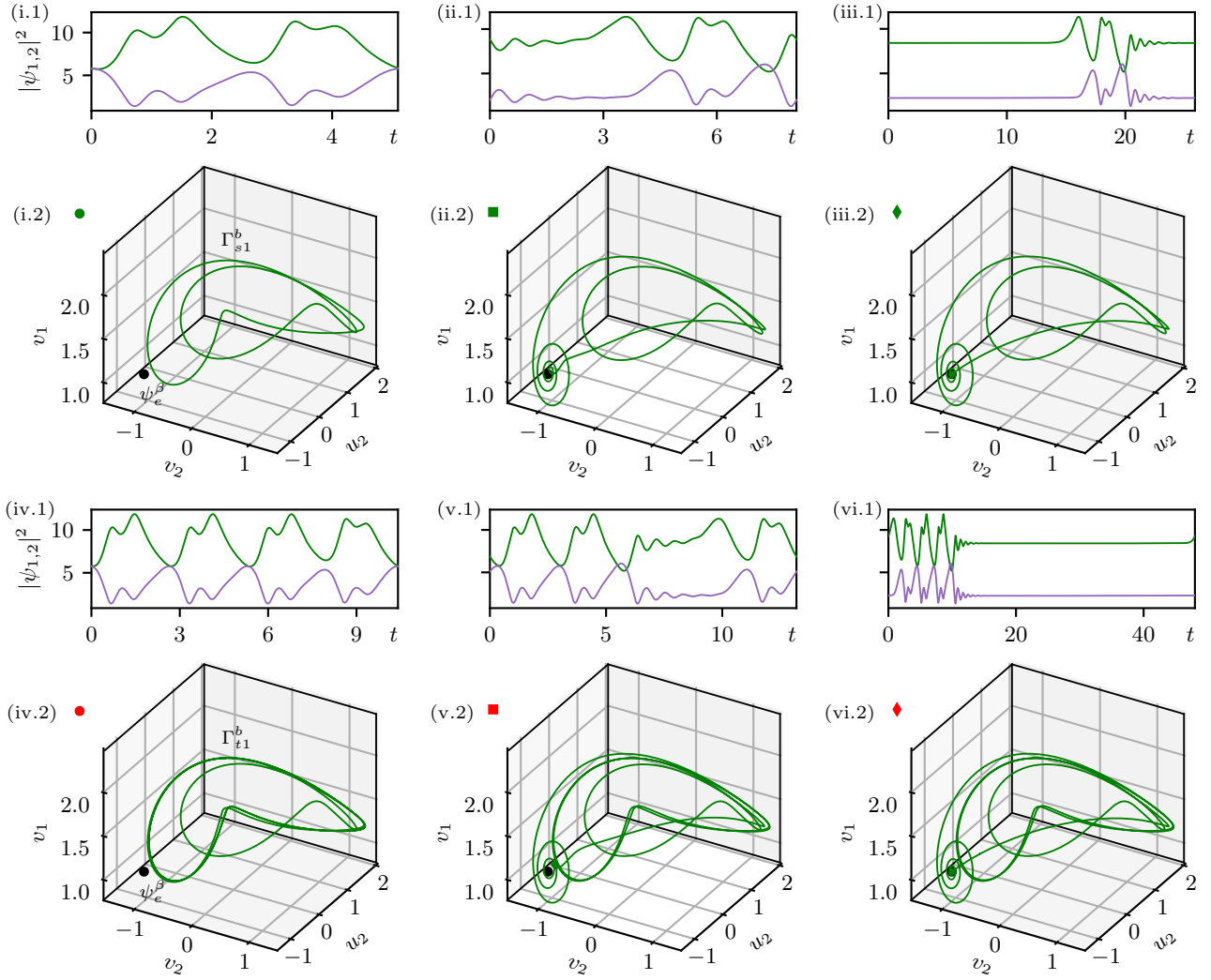


Figure 7. Temporal trace and projection on the $\{(v_2, u_2, v_1)\}$ -subspace of the subsidiary and tertiary oscillatory states Γ_b^{s1} and Γ_b^{t1} . Panels (i)-(iii) show the modification of Γ_b^{s1} along its bifurcation curve in Fig. 6(a) [see \bullet , \blacksquare , \blacklozenge]. At Hom_b^{s1} a 2-homoclinic orbit is created which is very similar to the state shown in (iii). Panels (iv)-(vi) show the modification of Γ_b^{t1} [see \bullet , \blacksquare , \blacklozenge] along its bifurcation curve while approaching Hom_{t1}^b in Fig. 6(d). At Hom_{t1}^b a 2-homoclinic orbit is created which is very similar to the state shown in (vi).

as a function of Δ , where T is the period of the oscillatory state. This allows us to better visualize the occurrence of the different Hom bifurcations.

Let us first take a look at the self-pulsing state Γ_b emerging from H_2^b . Soon after its birth, Γ_b undergoes a first PD bifurcation, and its norm $\|\psi\|$ changes in a damped oscillatory fashion while approaching asymptotically Hom_1^b [see Fig. 5(a)]. This structure corresponds to the spiral shown in the inset of Fig. 4(i), and each fold to an SNP. All along this curve, the period of Γ_b increases as approaching Hom_1^b , and in doing so, it describes the damped oscillatory curve in Δ plotted in Fig. 5(c). We refer to this state as *primary periodic* orbit [46].

In Fig. 6(a) we plot the bifurcation curve associated with the principal orbit Γ_b . Its modification along such a curve is depicted in Fig. 6(i)-(iii). In Fig. 6(i.1) we

show the temporal trace of Γ_b during one oscillatory period, and in Fig. 6(i.2) its 3D representation in the phase subspace $\{(v_2, u_2, v_1)\}$.

Moving down along this diagram, the period T of Γ_b increases [see Fig. 6(ii.1)], while the periodic attractor approaches the saddle-focus equilibrium ψ_e^β . In doing so, the periodic orbit temporarily follows the flow around ψ_e^β , leading to the almost spiral-like trajectory shown in Fig. 6(ii.2). Close to Hom_1^b , the periodic orbit looks like the one shown in Figs. 6(iii), where the oscillatory period has considerably increased, and where the orbit describes a spiral trajectory around ψ_e^β . The behavior of the trajectory around this point follows the unstable and stable manifolds of the SF equilibrium, being the latter one, responsible of the oscillatory tail shown in its temporal trace.

Label	ψ_e -type	Δ	λ_u	λ_s	δ
Hom_1^b	SF	11.7857	2.4078	-1 - $i7.9829j$	0.4153
Hom_{s1}^b	SF	11.8769	2.4282	-1 - $i8.0693$	0.4118
Hom_{s2}^b	SF	11.8216	2.4159	-1 - $i8.0166$	0.4139
Hom_{s3}^b	SF	11.8009	2.4113	-1 - $i7.9971$	0.4147
Hom_{t1}^b	SF	11.8804	2.4289	-1 - $i8.0727$	0.4116

Table I. Features and relevant information about the wild Shilnikov homoclinic bifurcations plotted in Fig. 6. SF stands for saddle-focus equilibrium, λ_s represents the stable eigenvalues, λ_u is unstable real eigenvalue, and δ is the saddle-index associated with the homoclinic bifurcation.

Approaching Hom_1^b , the period of Γ_b tends to infinite, and at that point, Γ_b collides with the SF equilibrium ψ_e^β , leading to the formation of the wild Shilnikov homoclinic orbit γ_b . This homoclinic orbit is very similar to the periodic orbit shown in Figs. 6(iii), however, for this set of parameters, it is unstable. The eigenvalues and saddle-index associated with this point are shown in Table I.

Very close to the SNPs, the primary bifurcation curve undergoes PD bifurcations [see \blacktriangledown in Fig. 6(a)], from where other *secondary* or *subsidiary* orbits emerge. The bifurcation curves associated with two of those secondary orbits Γ_b^{s0} and Γ_b^{s1} are plotted in green in Fig. 6(a).

The modification of the period-2 orbit Γ_b^{s1} around this diagram is shown in Fig. 7(i)-(iii). This orbit is well illustrated in Fig. 7(i.2). As in the single-period case, the period diverges as we descend the green diagram [see Fig. 7(ii.1)] and approach ψ_e^β . The vicinity of this equilibrium leads to the characteristic spiral trajectory shown in Fig. 7(ii.2). Further decreasing $|\psi|$, Γ_b^{s1} approaches Hom_{s1}^b , where it is destroyed and the homoclinic orbit γ_b^{s1} is created. This state is known as a *2-homoclinic orbit* and is very similar to the orbit plotted in Fig. 7(iii).

Similarly, secondary orbits of larger period arise from each of the PD bifurcations as one proceeds down in the diagram. Two of these curves are plotted in Figs. 6(b) and (c). Decreasing $|\psi|$, these orbits die at Hom_{s1}^b and Hom_{s2}^b , leading to new Shilnikov homoclinic orbits which occurs very close to Hom_1^b . The characteristics of these orbits are also shown in Table I. This phenomenon is known as *homoclinic doubling cascade* [44], and has been analyzed numerically in [49]. The main idea is that for $\Delta > \Delta_{\text{Hom}_1^b}$, an infinite number of N -homoclinic orbits γ_N (with $N > 0$) accumulate on the right side of the primary branch finishing at Hom_1^b .

The secondary green bifurcation curves $\Gamma_b^{s1,2,3}$ does also undergo PD bifurcation from where period-4 orbits emerge, leading to similar homoclinic doubling cascades. We represent this orbit as Γ_b^t , where the subindex t stands for *terciary*. The bifurcation curve associated with Γ_b^{t1} is shown in Fig. 6(d) together with Γ_b^{s1} . The modification of Γ_b^{t1} along this diagram is shown in Figs. 7(iv)-(vi). As proceeding down in the diagram, the modification of the orbits is similar to the single and period-2 cases. At Hom_{t1}^b a 4-homoclinic orbit is formed. This orbit is sim-

Label	ψ_e -type	Δ	λ_u	λ_s	δ
Hom_2^a	S	12.2951	1.1762	-3.1762	2.7003
Hom_2^b	S	12.2953	1.1134	-3.1134	2.7962
Hom_1^a	SF	12.9672	3.4932	-1 - $i9.7634$	0.28626
Hom_1^b	SF	13.2552	3.5641	-1 - $i1.0048$	0.28057

Table II. Features and relevant information about the homoclinic bifurcations are plotted in Fig. 8. SF stands for saddle-focus equilibrium, S corresponds to a saddle equilibrium, λ_s represents the stable eigenvalues, λ_u is an unstable real eigenvalue, and δ is the saddle-index associated with the homoclinic bifurcation.

ilar to the long period limit cycle plotted in Fig. 7(vi).

The limit cycle Γ_a emerging from H_2^a [see left red curve in Fig. 5(a)], also undergoes an oscillatory damped structure around Hom_1^a . However, the oscillations in Δ are more damped. The period of Γ_a diverges as approaching Hom_1^a , following the same oscillatory tendency [see Fig. 5(b)]. At Hom_1^a , the period of the oscillations becomes infinite, and Γ_a becomes the homoclinic orbit γ_a .

B. Saddle-Loop homoclinic bifurcation

Increasing S , the previous scenario is modified as illustrated in Fig. 8(a) for $S = 5.5$. Here, $\text{Hom}_1^{a,b}$ are closer to one another. Furthermore, close to H_2^a , Γ_a undergoes a series of SNP and PDs, which were absent before. The divergence of the period close to Hom_1^a is depicted in Fig. 8(b).

In contrast to the situation shown for $S = 4.5$, the bifurcation curve Γ_c emerging from Hom_1^b (in purple) does not connect with H_2^b , but with a new homoclinic bifurcation Hom_2^a taking place at the saddle equilibrium ψ_e^c . In this case [see a close-up view in Fig. 8(a)] the reconnection follows a monotonic growth in $|\psi|$ very different from the oscillatory one shown in the saddle-focus case. This saddle-loop homoclinic bifurcation, labeled Hom_2^a , is characterized by a scaling law $T \propto -\ln(\Delta - \Delta_{\text{Hom}_2^a})/a_u$, which governs the period of the oscillatory state very close to the bifurcation [7]. This divergence is plotted in Fig. 8(c).

The limit cycle Γ_b emerging from H_2^b does not die at Hom_1^b , but at another saddle-loop homoclinic bifurcation Hom_2^b . These homoclinic orbits are unstable, and therefore cannot be observed in direct numerical time simulations.

VI. CHAOTIC DYNAMICS

In this section, we analyze the emergence of chaotic dynamics, one close to $\Delta = C$, the other when $\Delta \gg C$, finding two main scenarios leading to chaos. The first one involves a period-doubling cascade [8], while the second one is associated with the presence of a homoclinic

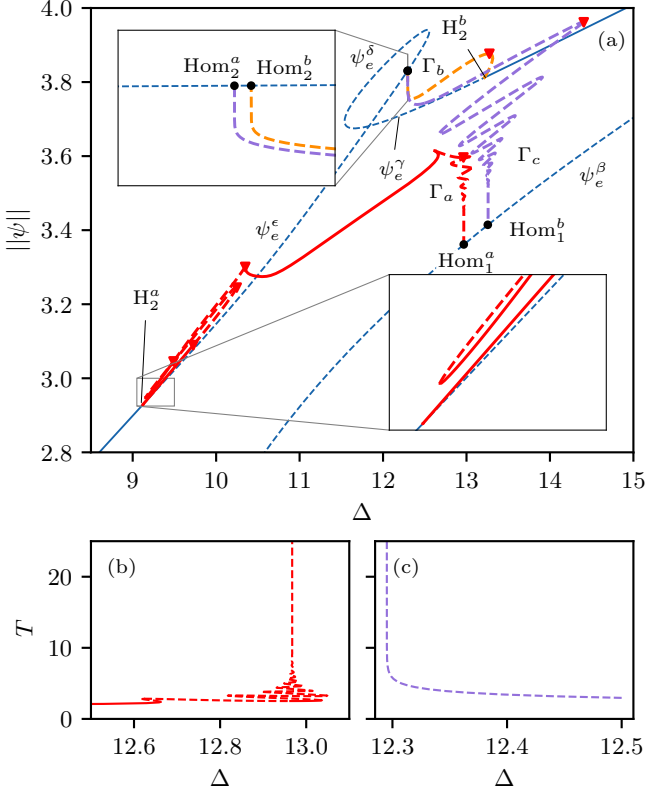


Figure 8. (a) Bifurcation diagram showing $||\psi||^2$ as a function of Δ around the Shilnikov bifurcations $Hom_1^{a,b}$ and saddle-loop bifurcations $Hom_2^{a,b}$ for $C = 5$ and $S = 5.5$. (b) shows the divergence of the period of Γ_a around Hom_1^a . (c) shows the monotonic divergence of the period of Γ_c when approaching Hom_1^a .

bifurcation [39].

A. Period doubling cascade to chaos

As shown previously, the periodic orbits emerging from the different H bifurcations may encounter PD bifurcations, where period-2 orbits are created, while the former ones become unstable. This PD process might repeat in cascade and then lead to temporal chaos. Figure 9(a) shows the occurrence of these bifurcations in a diagram which depicts $|\psi_1|^2$ as a function of S for $C = \Delta = 5$. This diagram corresponds to a vertical slice of the phase diagram shown in Fig. 4(a). We only plot the three equilibrium branches ψ_e^γ , ψ_e^δ , and ψ_e^ϵ , which are linked through the bifurcations SN_3^l and SN_3^r . The Hopf line H_1 cuts the stable branch at two points that we label $H_1^{a,b}$. From these points, the single period limit cycle Γ_a appears supercritically. The periodic attractor associated with this orbit is plotted in the 3D phase subspace $\{(v_2, u_2, v_1)\}$ depicted in Fig. 9(i.1). The temporal trace is shown in Fig. 9(i.2).

On the left, this state undergoes a pair of SNPs where

it loses and gains stability. Once SNP_2 is passed, Γ_a remains stable until PD_2 . This situation is shown in the close-up view plotted in Fig. 9(b). At PD_2 , an oscillatory state with two different periods, hereafter Γ_a^2 , emerges and remains stable until PD_4 . An example of this state is plotted in Fig. 9(ii). From PD_4 a new oscillatory state, Γ_a^4 , emerges [see Figs. 9(iii)] and after that, a cascade of period-doubling bifurcations (PD_8 , PD_{16} , etc) occurs in a very short interval of S . From these bifurcations, the states Γ_a^8 shown in Figs. 9(iv), and Γ_a^{16} (not shown here), emerge. Increasing a bit further S , the system reaches a regime characterized by chaotic states like the one shown in Fig. 9(v).

After passing PD_2 , Γ_a^2 undergoes several SNPs and PDs for increasing values of S , and eventually, it connects back to Γ_a . The different limit cycles undergo several SNPs as shown in the close-up view in Fig. 9(a). A similar structure is found on the right part of the diagram close to H_1^b .

The period-doubling cascades are also illustrated through the *Feigenbaum diagram* [8] plotted in Fig. 9(c). This diagram has been computed by scanning the stable attractors of the system as a function of S and collecting the local maxima and minima of the oscillatory states. The extension of this diagram corresponds to the shadowed gray box in Fig. 9(a). The close-up view corresponds to the range plotted in Fig. 9(b).

Increasing S , the chaotic attractor increases its morphological complexity and undergoes the typical windows of odd period oscillations [8]. A complete understanding of these modifications, and the *crisis* suffered by the attractor, requires the analysis of its return map, as reported in [50, 51]. The chaotic nature of this system can be also characterized through the computation of the Lyapunov exponent and the Kaplan-Yorke dimension associated with the dynamics. This type of approach has been applied to investigate the route to chaos in a plasmonic dimer [52]. Such analyses are beyond the scope of this work.

The chaotic dynamics persist until a critical value of S , where the chaotic attractor collides with an unstable periodic orbit on its basing boundary and is destroyed. This is a typical phenomenon in chaotic dynamics and it is known as *boundary crisis* [8]. We label this boundary crisis BC_1 as depicted in Fig. 9(a) and (c). After crossing this point, the only attractor of the system is the stable steady-state ψ_e^ϵ . Similarly, this route to chaos arises from H_1^b on the right and ends in a second BC_2 (not shown).

B. Chaos close to a Shilnikov homoclinic bifurcation

In this section, we analyze the emergence of chaotic dynamics close to homoclinic orbits. As stated by the Shilnikov theorem, if the Shilnikov bifurcation is wild (i.e. $\delta < 1$), chaotic dynamics is expected in the neighborhood of the homoclinic orbit [44]. The interplay be-

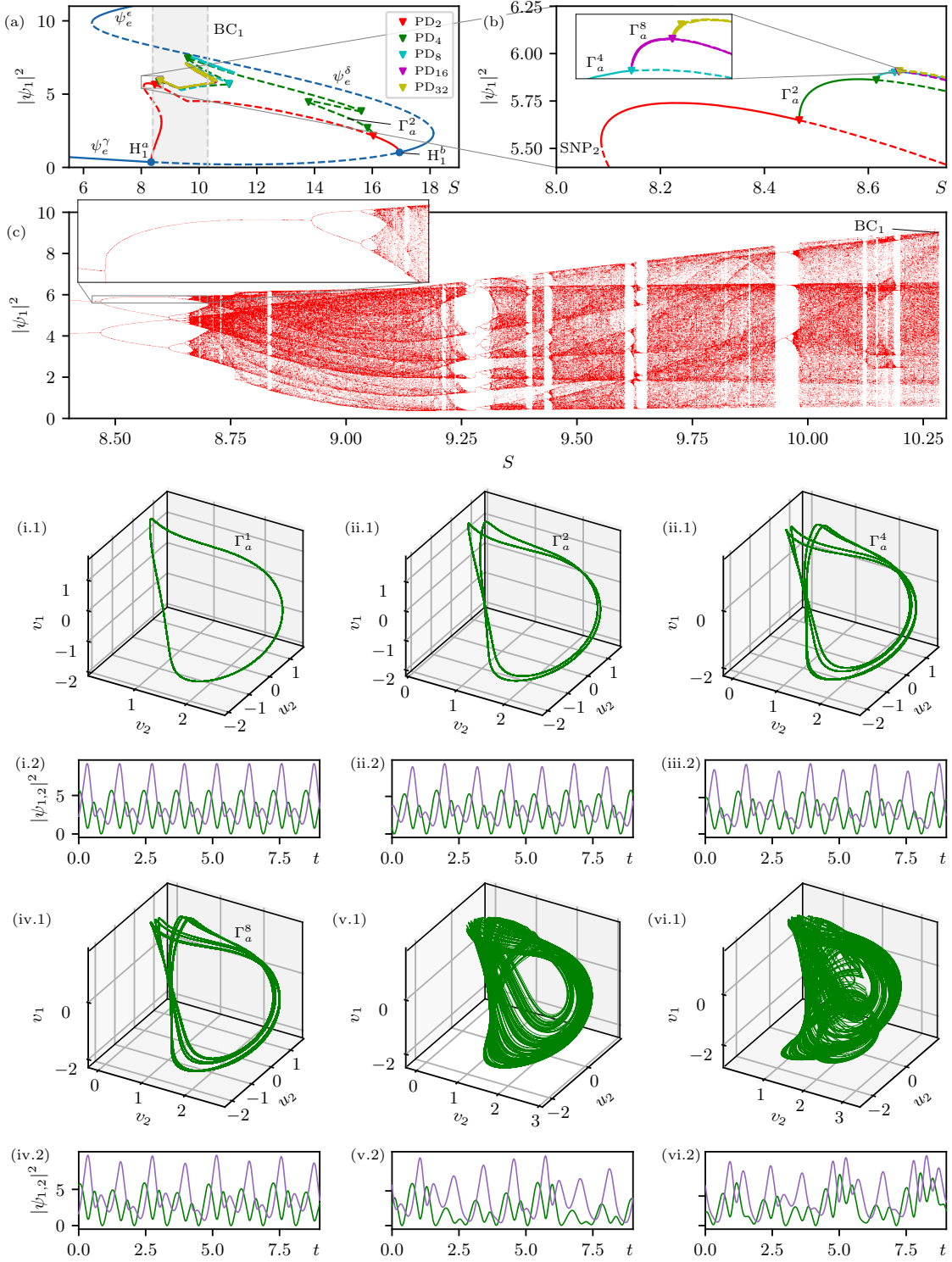


Figure 9. Period doubling cascade and route to chaos for $C = \Delta = 5$. (a) shows the modification of the norm $|\psi_1|^2$ as a function of S . The different colored branches correspond to the oscillatory states with different periodicities. We mark the Hopf bifurcations $H_1^{a,b}$ and different PD bifurcations. Solid (dashed) lines correspond to stable (unstable) states. Panel (b) is a close-up view of (a) around the period-doubling cascade. In (c) we plot the Feigenbaum diagram associated with the shadowed gray in (a), which shows the local maxima and minima modification of the dynamical attractors with changing S . Panels (i)-(vi) show the time trace (top panel) and projection of the attractors on the $\{(v_2, u_2, v_1)\}$ -subspace (bottom panels) for different values of S . From (i) to (vi) these values are respectively $S = 8.45, 8.50, 8.64, 8.84, 9.10, 10.26$. (v) and (vi) are chaotic attractors.

tween chaotic dynamics and homoclinic orbits has been studied by different authors, in particular in the context

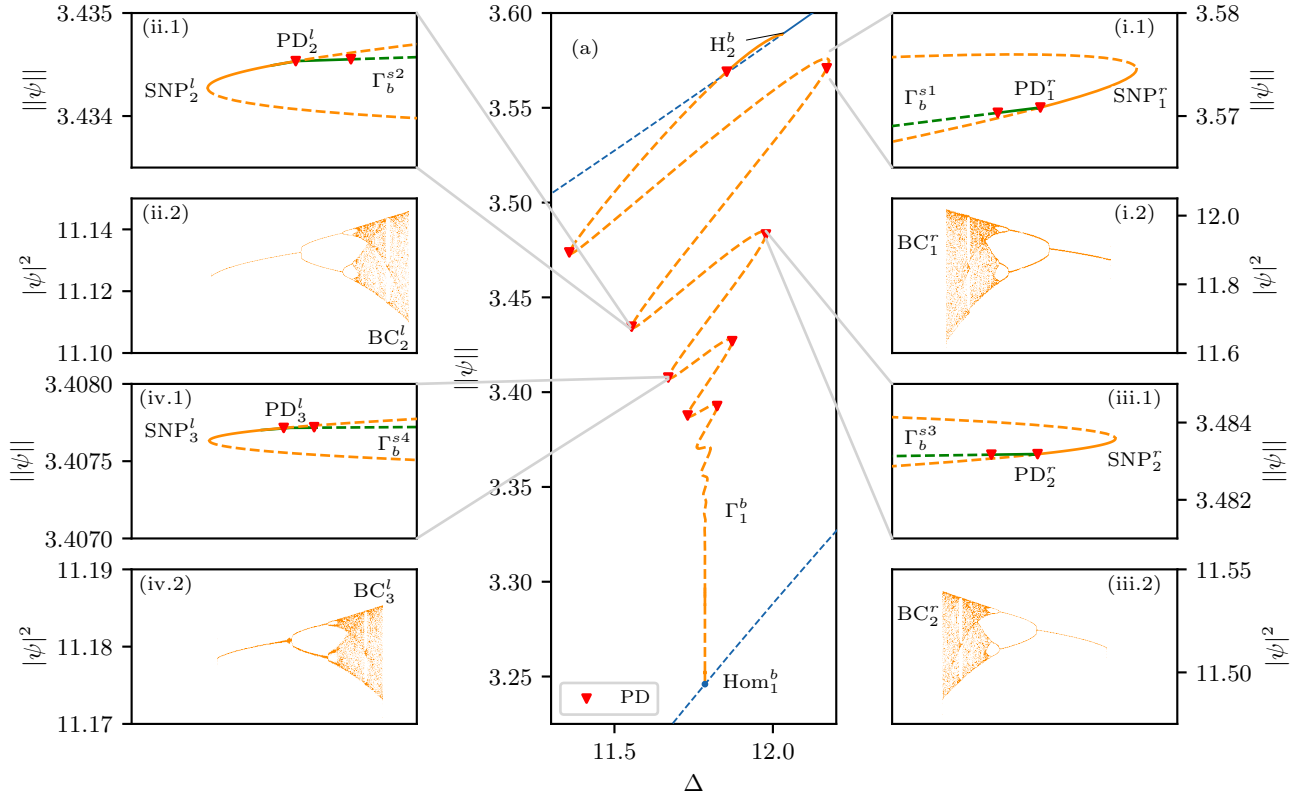


Figure 10. Period doubling route to chaos near a wild Shilnikov homoclinic orbit. (a) shows the bifurcation curve of the principal periodic orbit Γ_b emerging from H_2^b and dying at Hom_1^b . Panels (i.1)-(iv.1) show a close-up view of (a) around SNP_1^r , SNP_2^l , SNP_2^r and SNP_3^l , and the subsidiary dynamical state branches Γ_b^{s1-s4} . Panels (i.2)-(iv.2) show the Feigenbaum diagram and standard period-doubling route to chaos corresponding to the same branches. The chaotic states die at several boundary crises $\text{BC}_j^{l,r}$.

of the Rossler model [46, 53–55].

To illustrate this phenomenon here, let us take a look at the curve shown in Fig. 10, which corresponds to the primary orbit Γ_b emerging from H_2^b and dying at Hom_1^b . This diagram is a detailed version of the one plotted in Figs. 5(a) and 6(a). The close-up views of the diagram around the first four SNPs are shown in the insets, together with the PD bifurcations $\text{PD}_j^{l,r}$, and the period-2 secondary branches emerging from them. These plots show a similar structure for the left and right folds and extend along with the whole diagram with decreasing $\|\psi\|$ (not shown here for simplicity). The panels below show the Feigenbaum diagrams for the same interval in S and the period-doubling cascade. The agreement between both diagrams on the onset for the period-2 bifurcations is excellent. With increasing S , each of these attractors undergoes a BC, and they disappear.

All along this diagram, $\text{SNP}_i^{l,r}$ and $\text{BC}_i^{l,r}$ accumulate asymptotically around Hom_1^b , and so do the chaotic regions. Eventually, the left and right BCs may collide, leading to the merging of the left and right chaotic attractors very close to Hom_1^b . Furthermore, while decreasing $\|\psi\|$ and approaching Hom_1^b , the chaotic attractor comes closer and closer to the SF ψ_e^β , and the trajectories must

start to spiral around this point following the stable and unstable manifolds of ψ_e^β , in a similar manner as the one shown in Fig. 6 and Fig. 7 for the homoclinic orbits. The type of chaos associated with these attractors is commonly known as *spiral chaos* [54, 55]. However, due to the exponentially shrinking of the chaotic intervals when approaching Hom_1^b we have not been able to confirm these two hypotheses.

VII. DISCUSSIONS AND CONCLUSIONS

In this paper, we have presented a systematic study of the temporal dynamics arising in the asymmetrically-driven dissipative photonic Bose-Hubbard dimer model. This model has proved to describe excellently the self-pulsing dynamics of two coupled cavities [25]. The particularity of this system is that only one cavity is driven. This asymmetry in the driving leads to an absence of equivalent states (emerging from Pitchfork bifurcations) which are present in symmetrically driven cavities. [34]

Applying methods of dynamical systems and bifurcation theory we have presented a detailed collection of results describing the temporal dynamics of this system

in different regimes of operation.

After introducing the model in Sec. II, we have analyzed the modification of the resonances of the cavity, i.e. the homogenous states of the system, as a function of the driving field amplitude S , for two different coupling regimes (see Sec. III). We have referred to these regimes as weakly and strongly coupled regimes (WC and SC, respectively). The next step in this study has consisted in analyzing the linear stability of the homogeneous equilibrium points ψ_e against small perturbations. This analysis has been performed numerically using AUTO-07p [38]. The main steady-state bifurcations are depicted in Fig. 2. Through this analysis, we have detected Hopf bifurcations where ψ_e states are destabilized in favor of periodically oscillating ones. The main dynamical regimes of the system for the WC regime have been summarized in Fig. 3.

The continuation of oscillatory states has also been performed using AUTO-07p, as well as the computation of their stability [38]. This analysis has led to identifying PD cascades leading to limit cycles with different even periods. The periodic states may also undergo homoclinic bifurcations where they are destroyed.

We have proceeded similarly for the SC coupling regime ($C = 5$), and our findings show a much more complex dynamical scenario which is depicted in Fig. 4. In contrast to the WC case, here we have found two distinct oscillatory regimes, each one appearing close to one of the two nonlinear resonances of the cavity and [see Fig. 4(v)] For this value of C , these two regimes are disconnected. We have also shown that the limit cycles emerging from the right resonance encounter a variety of homoclinic bifurcations where they die.

In Sec. V we performed a systematic study of the homoclinic bifurcations appearing in the SC regime. To do so we have applied well-known results of dynamical systems theory [7]. We have identified two main types of homoclinic. One of them is a closed orbit bi-asymptotic to a saddle-focus equilibrium (i.e., Shilnikov homoclinic

orbits), while the other one connects a saddle point with itself. The main dynamical implications of both scenarios are described in detail.

Finally, we have also analyzed the chaotic behavior emerging in the system (see Sec. VI). Chaotic dynamics emerge through several period-doubling cascades which occur either close to a homoclinic bifurcation or far from it. The period-doubling cascade and its dynamics has been analyzed using continuation algorithms and direct numerical simulations. One example of the bifurcation structure of such states is presented in Fig. 9 (see Sec. VIA) together with a 3D representation of their different attractors.

We have also analyzed the emergence of chaotic dynamics close to the Shilnikov homoclinic bifurcations (see Sec. VIB). The main results are depicted in Fig. 10. In any case, the period-doubling cascade follows the typical Feigenbaum diagram [8].

The complexity of the dynamics appearing in this model, and the fidelity of our model to describe coupled Kerr cavities suggest that those dynamical regimes may be reachable experimentally. Hence, we hope that these results will be relevant for experimentalists working on these types of systems.

ACKNOWLEDGEMENTS

This work was supported by the Fonds de la Recherche Scientifique - FNRS under grant No PDR.T.0104.19 and the European Research Council (ERC) under the European Union's Horizon 2020 research and innovation program (grant agreement No 757800). F.L. and P.P.-R. acknowledge the support of the Fonds de la Recherche Scientifique-FNRS). P. P. -R acknowledges support from the European Union's Horizon 2020 research and innovation programme under the Marie Skłodowska-Curie grant agreement no. 101023717.

-
- [1] G. Nicolis, *Introduction to Nonlinear Science* (Cambridge University Press, Cambridge, England, 1995).
 - [2] A. Jenkins, Self-oscillation, *Phys. Rep.* **525**, 167 (2013).
 - [3] A. M. Zhabotinsky, A history of chemical oscillations and waves, *Chaos: An Interdisciplinary Journal of Nonlinear Science* **1**, 379 (1991).
 - [4] I. R. Epstein and J. A. Pojman, *An Introduction to Nonlinear Chemical Dynamics: Oscillations, Waves, Patterns, and Chaos* (Oxford University Press, 1998).
 - [5] J. R. Pomeroy, E. D. Sontag, and J. E. Ferrell, Building a cell cycle oscillator: hysteresis and bistability in the activation of Cdc2, *Nature Cell Biology* **5**, 346 (2003).
 - [6] J. Guckenheimer and P. J. Holmes, *Nonlinear Oscillations, Dynamical Systems, and Bifurcations of Vector Fields*, Applied Mathematical Sciences (Springer-Verlag, New York, 1983).
 - [7] P. Glendinning, *Stability, Instability and Chaos* (Cambridge University Press, Cambridge, England, 1994).
 - [8] E. Ott, *Chaos in Dynamical Systems*, 2nd ed. (Cambridge University Press, Cambridge, 2002).
 - [9] E. N. Lorenz, Deterministic Nonperiodic Flow, *Journal of the Atmospheric Sciences* **20**, 130 (1963).
 - [10] V. Petrov, V. Gáspár, J. Masere, and K. Showalter, Controlling chaos in the Belousov-Zhabotinsky reaction, *Nature* **361**, 240 (1993).
 - [11] P. D. Drummond, K. J. McNeil, and D. F. Walls, Non-equilibrium transitions in sub/second harmonic generation, *Opt. Acta* **27**, 321 (1980).
 - [12] L. A. Lugiato, L. M. Narducci, D. K. Bandy, and C. A. Pennise, Breathing, spiking and chaos in a laser with injected signal, *Opt. Commun.* **46**, 64 (1983).
 - [13] T. L. Paoli and J. E. Ripper, Coupled longitudinal mode pulsing in semiconductor lasers, *Phys. Rev. Lett.* **22**,

- 1085 (1969).
- [14] B. Maes, M. Fiers, and P. Bienstman, Self-pulsing and chaos in short chains of coupled nonlinear microcavities, *Phys. Rev. A* **80**, 033805 (2009).
- [15] J. Petráček, Y. Eksjöglu, and A. Sterkhova, Simulation of self-pulsing in Kerr-nonlinear coupled ring resonators, *Opt. Commun.* **318**, 147 (2014).
- [16] V. Grigoriev and F. Biancalana, Resonant self-pulsations in coupled nonlinear microcavities, *Phys. Rev. A* **83**, 043816 (2011).
- [17] Y. Sato, Y. Tanaka, J. Upham, Y. Takahashi, T. Asano, and S. Noda, Strong coupling between distant photonic nanocavities and its dynamic control, *Nat. Photonics* **6**, 56 (2012).
- [18] M. T. M. Woodley, L. Hill, L. Del Bino, G.-L. Oppo, and P. Del'Haye, Self-switching kerr oscillations of counterpropagating light in microresonators, *Phys. Rev. Lett.* **126**, 043901 (2021).
- [19] F. Bessin, F. Copie, M. Conforti, A. Kudlinski, A. Musot, and S. Trillo, Real-Time Characterization of Period-Doubling Dynamics in Uniform and Dispersion Oscillating Fiber Ring Cavities, *Phys. Rev. X* **9**, 41030 (2019).
- [20] M. Virte, K. Panajotov, H. Thienpont, and M. Sciamanna, Deterministic polarization chaos from a laser diode, *Nat. Photonics* **7**, 60 (2013).
- [21] A. Tikan, J. Riemensberger, K. Komagata, S. Hönl, M. Churaev, C. Sheadan, H. Guo, R. N. Wang, J. Liu, P. Seidler, and T. J. Kippenberg, Emergent nonlinear phenomena in a driven dissipative photonic dimer, *Nat. Phys.* **17**, 604 (2021).
- [22] X. Xue, Y. Xuan, P.-H. Wang, Y. Liu, D. E. Leaird, M. Qi, and A. M. Weiner, Normal-dispersion microcombs enabled by controllable mode interactions, *Laser Photonics Rev.* **9**, L23 (2015).
- [23] S. Fujii, Y. Okabe, R. Suzuki, T. Kato, A. Hori, Y. Honda, and T. Tanabe, Analysis of Mode Coupling Assisted Kerr Comb Generation in Normal Dispersion System, *IEEE Photonics J.* **10**, 1 (2018).
- [24] N. Carlon Zambon, S. R. K. Rodriguez, A. Lemaître, A. Harouri, L. Le Gratiet, I. Sagnes, P. St-Jean, S. Ravets, A. Amo, and J. Bloch, Parametric instability in coupled nonlinear microcavities, *Phys. Rev. A* **102**, 023526 (2020).
- [25] J. Yelo-Sarrión, P. Parra-Rivas, N. Englebort, C. M. Arabí, F. Leo, and S.-P. Gorza, Self-pulsing in driven-dissipative photonic Bose-Hubbard dimers, *Phys. Rev. Research* **3**, L042031 (2021).
- [26] M. Abbarchi, A. Amo, V. G. Sala, D. D. Solnyshkov, H. Flayac, L. Ferrier, I. Sagnes, E. Galopin, A. Lemaître, G. Malpuech, and J. Bloch, Macroscopic quantum self-trapping and Josephson oscillations of exciton polaritons, *Nat. Phys.* **9**, 275 (2013).
- [27] C. Bruder, R. Fazio, and G. Schön, The Bose-Hubbard model: from Josephson junction arrays to optical lattices, *Ann. Phys.* **14**, 566 (2005).
- [28] A. S. Kowligy, H. Timmers, A. J. Lind, U. Elu, F. C. Cruz, P. G. Schunemann, J. Biegert, and S. A. Diddams, Infrared electric field sampled frequency comb spectroscopy, *Science Advances* **5**, 36 (2019).
- [29] Z. L. Newman, V. Maurice, T. Drake, J. R. Stone, T. C. Briles, D. T. Spencer, C. Fredrick, Q. Li, D. Westly, B. R. Ilic, B. Shen, M.-G. Suh, K. Y. Yang, C. Johnson, D. M. S. Johnson, L. Hollberg, K. J. Vahala, K. Srinivasan, S. A. Diddams, J. Kitching, S. B. Papp, and M. T. Hummon, Architecture for the photonic integration of an optical atomic clock, *Optica* **6**, 680 (2019).
- [30] F. Leo, S. Coen, P. Kockaert, S. P. Gorza, P. Emplit, and M. Haelterman, Temporal cavity solitons in one-dimensional Kerr media as bits in an all-optical buffer, *Nat. Photonics* **4**, 471 (2010).
- [31] M. Zhang, C. Wang, Y. Hu, A. Shams-Ansari, T. Ren, S. Fan, and M. Lončar, Electronically programmable photonic molecule, *Nat. Photonics* **13**, 36 (2019).
- [32] J. Feldmann, N. Youngblood, C. D. Wright, H. Bhaskaran, and W. H. Pernice, All-optical spiking neurosynaptic networks with self-learning capabilities, *Nature* **569**, 208 (2019).
- [33] M. Kues, C. Reimer, P. Roztocky, L. R. Cortés, S. Sciara, B. Wetzel, Y. Zhang, A. Cino, S. T. Chu, B. E. Little, D. J. Moss, L. Caspani, J. Azaña, and R. Morandotti, On-chip generation of high-dimensional entangled quantum states and their coherent control, *Nature* **546**, 622 (2017).
- [34] A. Giraldo, B. Krauskopf, N. G. R. Broderick, J. A. Levenson, and A. M. Yacomotti, The driven-dissipative Bose-Hubbard dimer: phase diagram and chaos, *New J. Phys.* **22**, 043009 (2020).
- [35] L. A. Lugiato and R. Lefever, Spatial dissipative structures in passive optical systems, *Phys. Rev. Lett.* **58**, 2209 (1987).
- [36] E. J. Doedel, H. B. Keller, and J. P. Kernevez, Numerical analysis and control of bifurcation problems (i): bifurcation in finite dimensions, *Int. Journal Bifurcation Chaos Appl. Sci. Eng.* **01**, 493 (1991).
- [37] E. J. Doedel, H. B. Keller, and J. P. Kernevez, Numerical analysis and control of bifurcation problems (ii): bifurcation in finite dimensions, *Int. Journal Bifurcation Chaos Appl. Sci. Eng.* **1**, 745 (1991).
- [38] E. J. Doedel, B. E. Oldeman, A. R. Champneys, F. Dercole, T. Fairgrieve, Y. A. Kuznetsov, R. Paffenroth, B. Sandstede, X. Wang, and C. Zhang, AUTO-07p: Software for continuation and bifurcation problems in ordinary differential equations, *Department of Computer Science, Concordia University, Montreal* (2007).
- [39] S. Wiggins, *Introduction to Applied Nonlinear Dynamical Systems and Chaos*, 2nd ed. (Springer, New York, 2003).
- [40] J. Prat, I. Mercader, and E. Knobloch, The 1:2 mode interaction in Rayleigh-Bénard convection with and without Boussinesq symmetry, *Int. J. Bifurcation and Chaos Appl. Sci. Eng.* **12**, 281 (2002).
- [41] K. Bold, C. Edwards, J. Guckenheimer, S. Guharay, K. Hoffman, J. Hubbard, R. Oliva, and W. Weckesser, The Forced van der Pol Equation II: Canards in the Reduced System, *SIAM Journal on Applied Dynamical Systems* **2**, 570 (2003).
- [42] E. M. Izhikevich, Neural excitability, spiking and bursting, *Int. J. Bifurcation Chaos Appl. Sci. Eng.* **10**, 1171 (2000).
- [43] P. Parra-Rivas, D. Gomila, M. A. Matías, P. Colet, and L. Gelens, Competition between drift and spatial defects leads to oscillatory and excitable dynamics of dissipative solitons, *Phys. Rev. E* **93**, 012211 (2016).
- [44] A. J. Homburg and B. Sandstede, *Homoclinic and heteroclinic bifurcations in vector fields* (2010).
- [45] A. Champneys, Y. A. Kuznetsov, and B. Sandstede, A numerical toolbox for homoclinic bifurcation analysis, *Int. J. Bifurcation Chaos Appl. Sci. Eng.* **06**, 867 (1996).

- [46] P. Glendinning and C. Sparrow, Local and global behavior near homoclinic orbits, *Journal of Statistical Physics* **35**, 645 (1984).
- [47] D. Sarchi, I. Carusotto, M. Wouters, and V. Savona, Coherent dynamics and parametric instabilities of microcavity polaritons in double-well systems, *Phys. Rev. B* **77**, 125324 (2008).
- [48] C. Laing and P. Glendinning, Bifocal homoclinic bifurcations, *Physica D* **102**, 1 (1997).
- [49] B. E. Oldeman, B. Krauskopf, and A. R. Champneys, Death of period-doublings: locating the homoclinic-doubling cascade, *Physica D* **146**, 100 (2000).
- [50] O. E. Rössler, Chaos in abstract kinetics: Two prototypes, *Bulletin of Mathematical Biology* **39**, 275 (1977).
- [51] R. Barrio, F. Blesa, and S. Serrano, Qualitative analysis of the Rössler equations: Bifurcations of limit cycles and chaotic attractors, *Physica D* **238**, 1087 (2009).
- [52] Z. Ziani, G. Lévêque, S. Coulibaly, A. Taki, and A. Akjouj, Investigating Route to Chaos in Nonlinear Plasmonic Dimer, *Ann. Phys.* **532**, 2000240 (2020).
- [53] A. Arneodo, P. Coulet, and C. Tresser, Oscillators with chaotic behavior: An illustration of a theorem by Shil'nikov, *Journal of Statistical Physics* **27**, 171 (1982).
- [54] P. Gaspard and G. Nicolis, What can we learn from homoclinic orbits in chaotic dynamics?, *Journal of Statistical Physics* **31**, 499 (1983).
- [55] S. Malykh, Y. Bakhanova, A. Kazakov, K. Pusuluri, and A. Shilnikov, Homoclinic chaos in the Rössler model, *Chaos: An Interdisciplinary Journal of Nonlinear Science* **30**, 113126 (2020).